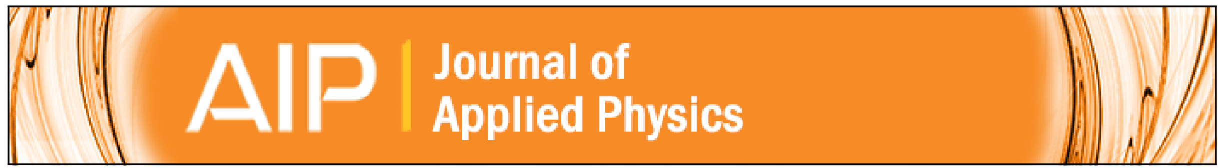

Quantifying carrier recombination at grain boundaries in multicrystalline silicon wafers through photoluminescence imaging

H. C. Sio, T. Trupke, and D. Macdonald

Citation: Journal of Applied Physics **116**, 244905 (2014); doi: 10.1063/1.4904963
View online: http://dx.doi.org/10.1063/1.4904963
View Table of Contents: http://scitation.aip.org/content/aip/journal/jap/116/24?ver=pdfcov
Published by the AIP Publishing

Articles you may be interested in
Transient photoluminescence from silicon wafers: Finite element analysis
J. Appl. Phys. **114**, 163105 (2013); 10.1063/1.4826896

Imaging crystal orientations in multicrystalline silicon wafers via photoluminescence
Appl. Phys. Lett. **101**, 082102 (2012); 10.1063/1.4747801

Capability of photoluminescence for characterization of multi-crystalline silicon
J. Appl. Phys. **111**, 073504 (2012); 10.1063/1.3699275

Spatially resolved modeling of the combined effect of dislocations and grain boundaries on minority carrier lifetime in multicrystalline silicon
J. Appl. Phys. **101**, 053515 (2007); 10.1063/1.2435815

Surface recombination velocity of silicon wafers by photoluminescence
Appl. Phys. Lett. **86**, 112110 (2005); 10.1063/1.1884258

[This article is copyrighted as indicated in the article. Reuse of AIP content is subject to the terms at: http://scitation.aip.org/termsconditions. Downloaded to] IP: 130.56.107.192 On: Thu, 29 Jan 2015 19:35:37

JOURNAL OF APPLIED PHYSICS 116, 244905 (2014)

Quantifying carrier recombination at grain boundaries in multicrystalline silicon wafers through photoluminescence imaging

H. C. Sio,[1,a)] T. Trupke,[2] and D. Macdonald[1]

[1]*Research School of Engineering, The Australian National University (ANU), Canberra ACT 0200, Australia*
[2]*BT Imaging Pty Ltd, Waterloo, New South Wales 2017, Australia*

(Received 14 September 2014; accepted 11 December 2014; published online 29 December 2014)

We present a method based on steady state photoluminescence (PL) imaging and modelling of the PL intensity profile across a grain boundary (GB) using 2D finite element analysis, to quantify the recombination strength of a GB in terms of the effective surface recombination velocity (S_{eff}). This quantity is a more meaningful and absolute measure of the recombination activity of a GB compared to the commonly used signal contrast, which can strongly depend on other sample parameters, such as the intra-grain bulk lifetime. The method also allows the injection dependence of the S_{eff} of a given GB to be explicitly determined. The method is particularly useful for studying the responses of GBs to different cell processing steps, such as phosphorus gettering and hydrogenation. The method is demonstrated on double-side passivated multicrystalline wafers, both before and after gettering, and single-side passivated wafers with a strongly non-uniform carrier density profile depth-wise. Good agreement is found between the measured PL profile and the simulated PL profile for both cases. We demonstrate that single-side passivated wafers allow more recombination active grain boundaries to be analysed with less unwanted influence from nearby features. The sensitivity limits and other practical constraints of the method are also discussed. © *2014 AIP Publishing LLC*. [http://dx.doi.org/10.1063/1.4904963]

I. INTRODUCTION

Multicrystalline silicon (mc-Si) is one of the most commonly used materials for solar cell applications. While being lower cost, mc-Si solar cells generally have lower efficiency compared to mono-crystalline silicon materials due to higher impurity concentrations and the presence of crystal defects in the materials. Grain Boundaries (GBs) are one type of crystal defect which significantly affects the efficiency of mc-Si solar cells. They can act as strong recombination centres for carriers and hence can locally reduce the minority carrier lifetime. Accurate measurement of the electrical properties of GBs is essential for developing methods to reduce their impact and therefore improving the performance of mc-Si solar cells.

The electrical properties of GBs depend strongly on the degree of symmetry or misorientation between the neighbouring grains forming the GBs. Several works have correlated the recombination strength of GBs with the coincidence site lattice (CSL) GB type.[1–3] The recombination strength of GBs depends not only on the atomic coincidence but also the contamination level in the material. Buonassisi *et al.*[4] showed that metal silicide precipitates are more likely to form at GBs with lower atomic coincidence. Chen *et al.*[2] observed a large variation of recombination strength among different types of GBs in heavy contaminated wafers compared to clean or lightly contaminated wafers, in which only a small variation can be observed. Moreover, it has been shown that the electrical properties of GBs change after phosphorous gettering[5,6] and hydrogenation.[7,8] However, the underlying mechanisms are not fully understood yet. Karzel *et al.*[1] studied different CSL GBs before and after phosphorous gettering and hydrogenation in wafers cut from two individual mc-Si ingots and observed a distinct difference in the GBs from those two ingots in terms of their as grown properties and their responses to gettering and hydrogenation.

The majority of previous works have used signal contrast, which is defined as the ratio of the intensity of the photoluminescence (PL) or electron beam induced current (EBIC) signal between the GB and the intra-grain region, to evaluate and compare GBs. Signal contrast is straightforward and easy to calculate, thus allowing a large number of GBs to be studied. However, it only provides evaluation of the recombination strength on a relative scale and depends on the lifetime of the intra-grain region, which is likely to vary at different injection levels, among different wafers, or during cell processing steps. As signal contrast is only a relative and qualitative representation, it also prohibits a direct comparison of results from previous work. We have previously[3] attempted to quantify the recombination properties of GBs quantitatively through calculating the recombination current induced by GBs, based on an approach proposed by Augarten *et al.*[9] for calculating shunt currents. This reflects the effective detrimental influence of a GB in a mc-Si wafer when it is illuminated, similar to a solar cell under normal operation. Nevertheless, such a parameter might be misleading in representing the electrical properties of a GB as it depends not only on the GB itself but also strongly on other parameters such as the carrier generation rate and the lifetime of the grains near the GB. In order to clarify the root cause of the varying recombination behaviour of GBs, it is

[a)]Author to whom correspondence should be addressed. Electronic mail: kelvin.sio@anu.edu.au. Tel.: +61 2 6195 0078. Fax: +61 2 6125 0506.

 © 2014 AIP Publishing LLC

[This article is copyrighted as indicated in the article. Reuse of AIP content is subject to the terms at: http://scitation.aip.org/termsconditions. Downloaded to] IP: 130.56.107.192 On: Thu, 29 Jan 2015 19:35:37

more meaningful to evaluate the intrinsic recombination properties of GBs, which are independent of the measurement conditions or other sample parameters.

Donolato[10,11] presented an analytical model to describe the recombination properties of GBs and dislocations in terms of interface recombination velocity and line recombination velocity. The works were further extended by Riepe *et al.*[12] and Stokkan *et al.*,[13] who modelled the effect of various GBs and dislocations on minority carrier lifetime for Carrier Density Imaging (CDI) measurements, in terms of parameters such as grain boundary misorientation and capture cross section. Corkish *et al.*[14] and Micard *et al.*[15] proposed a direct fitting procedure based on analytical modelling to extract the effective surface recombination velocities (S_{eff}) of GBs and the diffusion length in the neighbouring grains from electron beam induced current (EBIC) and light beam induced current (LBIC) profiles across a GB. In this work, we present an approach based on the steady state photoluminescence (PL) imaging technique and 2D modelling of the PL intensity profile across a GB, to determine S_{eff} of a GB, which is a more meaningful and absolute measure of recombination activities than signal contrast or recombination current. PL imaging is a rapid, non-destructive and spatially resolved characterisation technique which has a variety of applications such as carrier lifetime imaging.[16] One major advantage of the PL imaging technique is that it does not require a cell structure or a pn junction, in contrast to EBIC or LBIC measurements, thus reducing the difficulty of sample preparation as well as the complexity of the modelling. In this paper, we have applied the presented method to two different types of samples. Firstly, the method is applied to determine S_{eff} of several GBs in double-side passivated mc-Si wafers, both before and after phosphorus gettering. Secondly, the method is applied to mc-Si wafers with infinite surface recombination at the rear surfaces, in order to enhance the sensitivity of the method to strongly recombination active GBs, as explained in detail below.

II. MODEL DESCRIPTION

Our presented model is a two dimensional simplification of a three dimensional problem, assuming no variation in the materials along the z-axis. Fig. 1(a) shows the schematic of our 2D model, illustrating the interactions between a GB and its neighbouring grains under steady state illumination. A GB, modelled as a surface with an effective surface recombination velocity (S_{eff}), is located between two neighbouring grains, G1 and G2 with bulk minority carrier lifetime $\tau_1(\Delta n)$ and $\tau_2(\Delta n)$, respectively. The semiconductor is subjected to a certain degree of surface recombination at both the front and rear surfaces, depending on the films on the surfaces, represented by S_{front} and S_{rear}. Both S_{front} and S_{rear} are considered to be injection independent in our model, as the surface recombination velocities are assumed to be either negligible or infinite, as explained further below. Here, we assume that the GB is perpendicular to the surfaces. The semiconductor is divided into multiple nodes in both x and y directions, as shown in Fig. 1(b). The local carrier concentration at each node is simulated using a finite difference

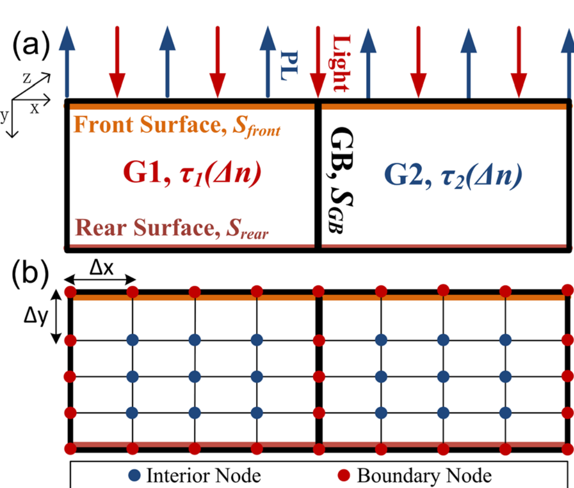

FIG. 1. (a) Schematic of the presented 2D model. (b) Grid structure of the semiconductor for finite element analysis.

method based on the continuity equation, allowing for local carrier generation, diffusion, and recombination. We then modelled the PL profile across a GB through the rate of spontaneous emission of electrons and holes via band-band transitions, considering reflection, reabsorption of the emitted PL and the quantum efficiency of the detector.

The simulated PL profile is a function of the incident photon flux, the reflectivity, thickness, and doping of the sample, the surface recombination velocity of the GB, the lifetimes of the neighbouring grains forming the GB and other instrument dependent parameters such as the quantum efficiency of the detector. All the parameters except S_{GB} can be measured directly. The injection dependent bulk lifetimes of the neighbouring grains are sample parameters required for the model and are extracted from PL calibrated lifetime images, as explained further below. A constant scaling factor K is used for correlating the modelled PL signal to the actual measured PL signal and is determined using the measured PL intensity of a spatially uniform region in the sample. Based on the model, we determine S_{eff} of a GB by fitting the simulated PL profile with the experimental profile, using the golden section search[17] with S_{GB} as the varying parameter. The details of the modelling and a list of parameters required for the fitting are given in the Appendix.

For samples with uniform carrier profiles depth-wise, it is possible to simply fit the modelled carrier density profile across a GB to the measured profile extracted from PL calibrated carrier density images, avoid the complexity of modelling the PL signal. Modelling the PL signal, however, allows the method to be applied to samples with non-uniform carrier profiles depth-wise, such as single-side passivated samples used in this work, which significantly broadens the applicability of the method, as explained further below.

III. EXPERIMENTAL METHOD

A. Sample preparation

Two groups of p-type boron doped mc-Si wafers were used in this work. Wafers from the first group were around

[This article is copyrighted as indicated in the article. Reuse of AIP content is subject to the terms at: http://scitation.aip.org/termsconditions. Downloaded to] IP: 130.56.107.192 On: Thu, 29 Jan 2015 19:35:37

180 μm thick and were cut from a commercially grown directionally solidified ingot. Wafers from the second group were cut from a different ingot, with a thickness of around 330 μm. All the wafers were further cut into smaller pieces, followed by a chemical etching using HF acid and HNO_3 to remove saw damage, and to create an optically planar surface. Having such a planar surface is necessary for our simplified modelling of the PL emission to be valid, with details described in the Appendix. Although the chemical etching can sometimes cause surface pits near GBs, these do not have a significant impact in the PL images. Sister wafers in the first group were further divided into two series. Wafers in the first series were phosphorous gettered and then received an aluminum oxide film deposited by plasma-assisted atomic layer deposition (PA-ALD) together with their non-gettered sister wafers. Sister wafers in the second group were all phosphorous gettered, then divided into two series. The first series received a silicon nitride film on both surfaces, while their sister wafers received silicon nitride film on the front surfaces and a thin metallic aluminum film on the rear surfaces using metal evaporation, to achieve instantaneous rear surface recombination conditions.[18] The surface recombination velocity at the rear surface (S_{rear}) is assumed to given by its maximum value, 3×10^6cm/s.[19] Silicon nitride films were deposited by plasma enhanced chemical vapour deposition (PECVD). The double-side passivated wafers were used to estimate the bulk lifetime for modelling, while the single-side passivated wafers were used to investigate GB behaviour.

B. PL imaging

PL images were captured with a BT Imaging LIS-R1 tool, in which an 808 nm laser is used for carrier excitation. The PL images used in this work have a pixel size of 22 μm. In addition to the long pass filter used to filter the reflected laser light, a short pass filter with a cut off wavelength of 1050 nm was placed in front of the detector to filter the emitted band-to-band PL signal. The use of a short pass filter reduces the impact of lateral light scattering both within the sample itself and within the camera's CCD chip on the captured PL images, therefore producing less blurred images. Image deconvolution using an experimentally determined point-spread function (PSF) was applied to the PL images to further reduce the impact of image blurring caused by crosstalk in the CCD chip. While the use of the short-pass filter reduces this effect,[20] it can still have some impact on the PL contrast profile across a GB.

As input parameters, our model requires the bulk lifetime of the neighbouring grains ($\tau_1(\Delta n), \tau_2(\Delta n)$) to be determined. The bulk lifetimes were measured in the intra-grain regions, far away from the GB, using the PL imaging technique. It was assumed that negligible surface recombination occurs at both the front and the rear surfaces as the wafers were well passivated with $S_{eff} < 10$ cm/s, verified by comparison with mono-crystalline control wafers. A series of PL images captured at different injection levels were used to determine their corresponding injection dependence. The PL images were calibrated into lifetime images based on an optically corrected calibration constant extracted from mono-crystalline calibration wafers, described in detail in Ref. 21. A recently proposed carrier de-smearing technique[22] was applied to the calibrated lifetime images to account for the influence of lateral carrier smearing within the sample and thus to allow more accurate extraction of the intra-grain lifetime.

IV. RESULTS

A. Double-side passivated sample before and after phosphorous gettering

Fig. 2 shows calibrated lifetime images of an as grown mc-Si wafer and a gettered sister wafer from the first group. Both images are taken with the same incident photon flux ($\phi = 2.3 \times 10^{17}$ cm^{-2}s^{-1}). Comparing Figs. 2(a) and 2(b), it can be seen that the lifetime of intra-grain regions improves after phosphorous gettering, due to the removal of impurities in the bulk. While some GBs become more recombination active, the opposite behaviour is observed in other GBs.

We extracted the PL intensity profiles across several selected GBs and fitted the simulated PL profiles according to the method described above to determine their corresponding

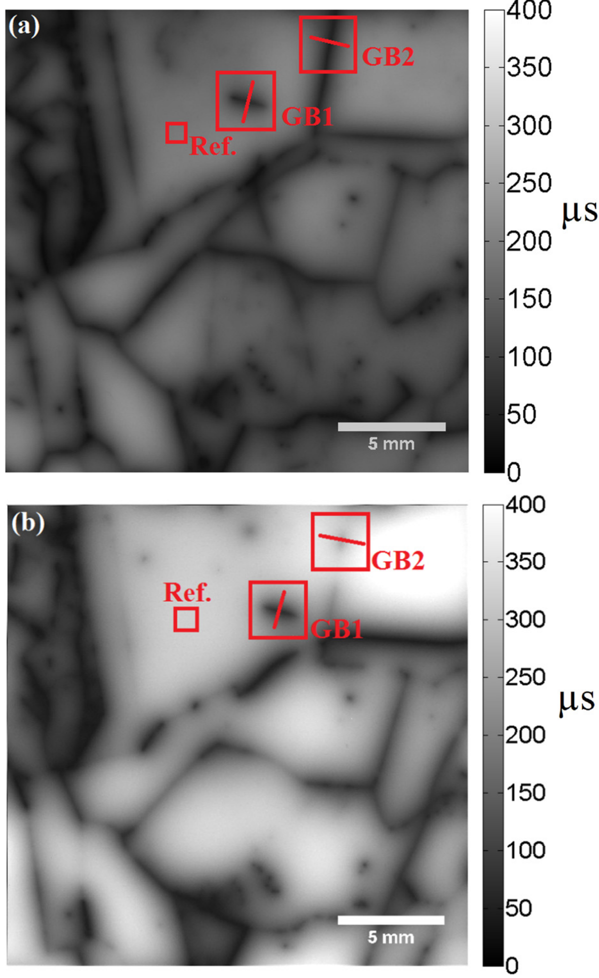

FIG. 2. Calibrated lifetime (in μs) image of (a) an as grown Al_2o_3 passivated mc-Si wafer (b) a gettered Al_2o_3 passivated sister wafer. The same scale is used for both images for direct comparison of the lifetime values. Ref. represents the reference region that is used for the calculation of the scaling factor K.

[This article is copyrighted as indicated in the article. Reuse of AIP content is subject to the terms at: http://scitation.aip.org/termsconditions. Downloaded to] IP: 130.56.107.192 On: Thu, 29 Jan 2015 19:35:37

S_{eff}. We first applied our model to study the response of two highlighted GBs (GB1 and GB2) to phosphorous gettering under the same photon excitation condition. The fitting result is shown in Figs. 3 and 4. The simulated PL profile agrees well with the measured PL profile, demonstrating the applicability of the method. The small discrepancy between simulated PL profile and the measured PL profile at regions very close to the GB might be due to optical artefacts, such as the focussing of the imaging lens or carrier smearing in the detector which has not been completely corrected for, which cause blurriness in the acquired images especially at sharp features such as a strongly recombination active GB. Our result shows that while the S_{eff} of GB1 increases from 890 cm/s to 1810 cm/s, the S_{eff} of GB2 decreases from 1130 cm/s to 230 cm/s after phosphorus gettering.

Note that the extracted S_{eff} value only represents the surface recombination velocity of a GB at a particular injection level. Even with the same generation rate, the excess carrier density at GBs can be different after gettering due to their variation in lifetime. To account for this, we applied our model to six individual PL images of each sample taken at different injection levels and determined S_{eff} of GB1 before and after gettering, as a function of injection level at the GB. We used our model simulated minority carrier density at the GB to represent the injection level at which the S_{eff} value was extracted. The result is shown in Fig. 5. GB1, in general, becomes more recombination active after gettering except at low injection ($\Delta n \ll 1 \times 10^{14}\,\mathrm{cm}^{-14}$), in which case the recombination strength is largely unchanged. Before gettering, GB1 exhibits a strong injection dependence, with S_{eff} decreasing significantly as injection level increases. This is similar to the recombination property of decorated dislocations, in which the enhancement in the recombination strength due to coulomb potential, created by the capture of majority carriers by electronic states at the dislocation, is thought to be reduced as the minority carrier concentration increases.[23] After gettering, the injection dependence is much less pronounced, suggesting a possible change in the origin of the recombination activity.

Note also the asymmetrical carrier profile on either side of the GB, as can be observed in Fig. 4, due to variation in the bulk lifetime between neighbouring grains. This variation can induce errors in signal contrast methods but does not impact the extracted injection dependent S_{eff} values. The injection dependent S_{eff} of a GB represents the intrinsic property of a GB and is independent of the lifetime of the neighbouring grains forming the GB. The lifetime of the neighbouring grains does not impact the recombination strength of a GB directly, but indirectly through affecting the carrier concentration at the GB due to the injection dependent nature of the recombination properties of a GB.

There are two main limitations in applying the proposed model to double-side passivated samples. Firstly, our method assumes that the extracted PL profile is not affected by the presence of other nearby electrically active structural defects, such as a second GB. This would require the selected GB to be located several diffusion lengths away from other recombination centres. This can be satisfied by selecting GBs located between two large grains. However, carrier diffusion lengths can reach 1 mm or above in well passivated samples, especially after gettering. This significantly limits the number of GBs that can be studied. Secondly, the injection dependent lifetime values of both

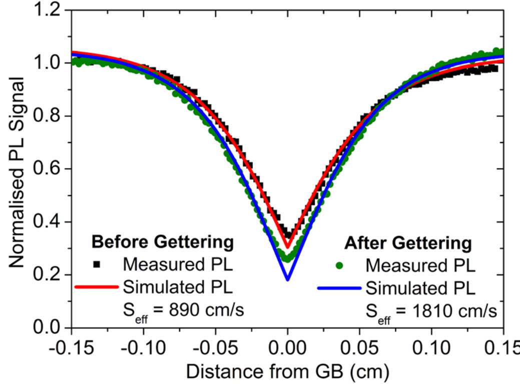

FIG. 3. Simulation fitting of GB1, as highlighted in Fig. 2, before and after gettering. The PL signal is normalised against the average PL signal of the highlighted reference region in Fig. 2, which is used for the calculation of the scaling factor K. Note that the normalisation factors for the PL profiles are different due to different lifetimes in the reference regions.

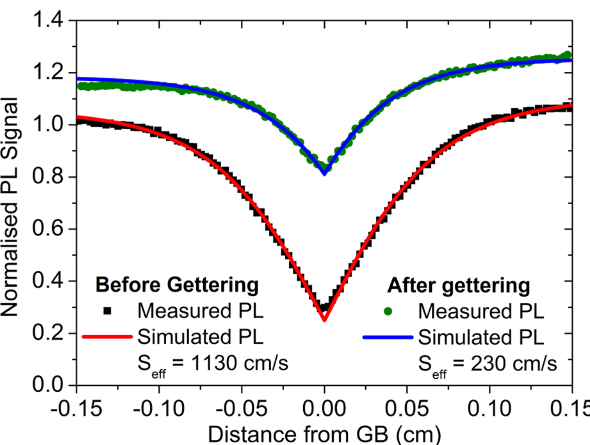

FIG. 4. Simulation fitting of GB2, as highlighted in Fig. 2, before and after gettering. The PL signal is normalised against the average PL signal of the highlighted reference region in Fig. 2, which is used for the calculation of the scaling factor K. Note that the normalisation factors for the PL profiles are different due to different lifetimes in the reference regions.

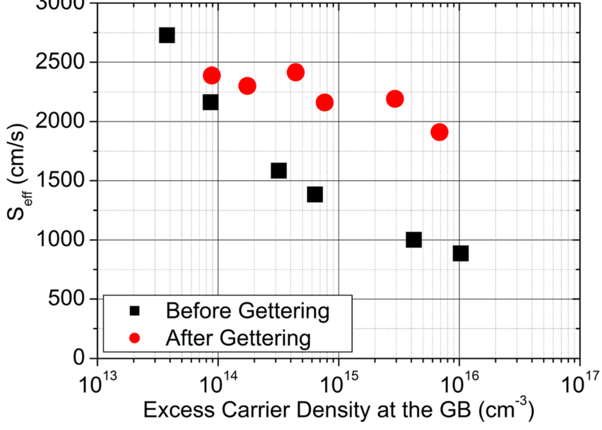

FIG. 5. Injection dependent S_{eff} of GB1, as highlighted in Fig. 2, before and after gettering.

[This article is copyrighted as indicated in the article. Reuse of AIP content is subject to the terms at: http://scitation.aip.org/termsconditions. Downloaded to] IP: 130.56.107.192 On: Thu, 29 Jan 2015 19:35:37

neighbouring grains are used as input parameters for the fitting. The quality of fit as well as the fitting result depends strongly on the accuracy of the intra-grain lifetime values used. The close proximity of other GBs can increase uncertainty in these lifetime values, which in turn can lead to a large uncertainty in the fitting result.

B. Single-side passivated sample

To account for the limitations stated above, we have also applied our model to single-side passivated mc-Si wafers with infinite surface recombination at the rear surfaces, achieved by evaporating a thin layer of aluminum. This significantly reduces the effective minority carrier diffusion length within the samples, hence allowing more closely spaced GBs to be studied. Moreover, this also reduces the sensitivity of the fitting on the intra-grain lifetime, as the carrier concentration on both sides of the GB is limited by carrier transport to the rear surface, due to the infinite rear surface recombination velocity. We chose to use mc-Si wafers with a thickness of around 330 μm instead of the more typical 180 μm wafers to allow for higher excess carrier densities inside the sample, which increases the signal to noise ratio in the PL measurements. This also allows a reasonable degree of carrier diffusion, preventing the region of influence of the GBs from becoming too narrow to be observed with the spatial resolution of the PL imaging setup.

Fig. 6 shows PL images of such a single-side passivated sample and a double-side passivated sister wafer, taken with the same incident photon flux ($\phi = 2.7 \times 10^{18}\ \mathrm{cm}^{-2}\mathrm{s}^{-1}$). The PL image of the single-side passivated sample is much sharper compared to the one in the double-side passivated case, due to a large reduction in the carrier smearing as a result of significantly shorter effective minority carrier diffusion lengths. The significant reduction in carrier smearing might also allow extending the work to characterise closely packed dislocation networks or loops, which are otherwise very difficult to study in well passivated samples due to the overlapping influence of multiple dislocations. Fig. 7 shows the measured PL profile and its corresponding profile fitting for GB3, highlighted in Fig. 6(a). The bulk lifetimes ($\tau_1(\Delta n), \tau_2(\Delta n)$) of the neighbouring grains are required for the profile fitting and were measured from a double-side passivated sister wafer, Fig. 6(b), after applying the carrier de-smearing technique.[22] Good agreement is found between the measured PL profile and the simulated PL profile, demonstrating that our model can be applied not only on well passivated samples but also on samples with strongly non-uniform carrier density profiles depth-wise, provided that the bulk properties and the boundary conditions are well known.

Fig. 8 compares injection dependent S_{eff} of GB3 extracted from a single-side passivated sample and a double-side passivated sister wafer. The extracted values agree reasonably well with each other. The small discrepancy may be due to one of the following reasons. Firstly, for the single-side passivated sample, due to the large variation in the carrier profiles at the GB, we adapted a weighted average carrier concentration ($\Delta n_{avg} = \frac{\int_0^\infty \Delta n^2 dx}{\int_0^\infty \Delta n dx}$), proposed by Bowden *et al.*[24] for determining lifetime in silicon bricks, to represent the average carrier concentration at the GB. Different averaging methods can lead to a different average value of the

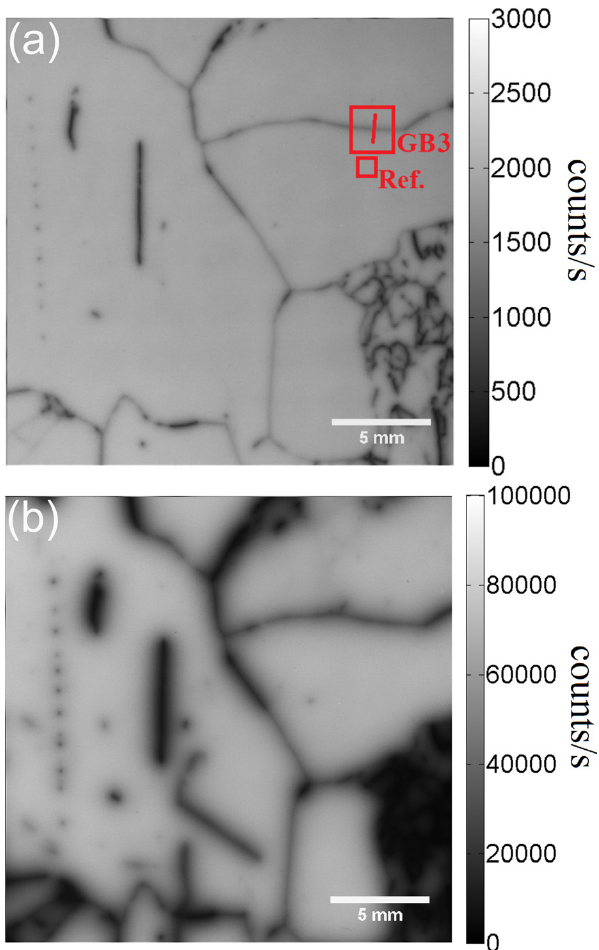

FIG. 6. PL image of a (a) single-side passivated mc-Si wafer (b) double-side passivated sister wafer. Ref. represents the reference region that is used for the calculation of the scaling factor K. The PL signal is normalised against the exposure time of each PL image. Note that the scales of the two images are different.

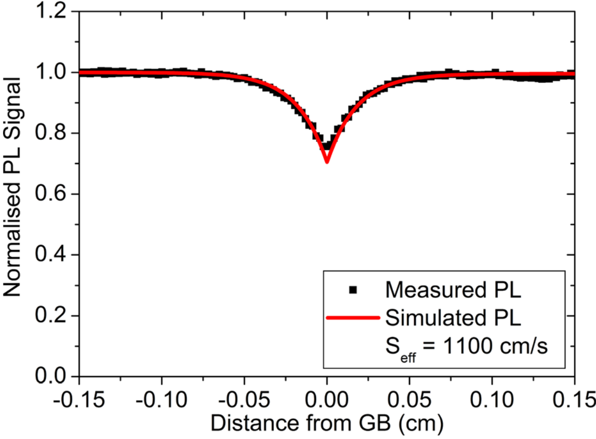

FIG. 7. Simulation fitting of GB3, as highlighted in Fig. 6(a). The PL signal is normalised against the average PL signal of the highlighted reference region in Fig. 6(a), which is used for the calculation of the scaling factor K.

[This article is copyrighted as indicated in the article. Reuse of AIP content is subject to the terms at: http://scitation.aip.org/termsconditions. Downloaded to] IP: 130.56.107.192 On: Thu, 29 Jan 2015 19:35:37

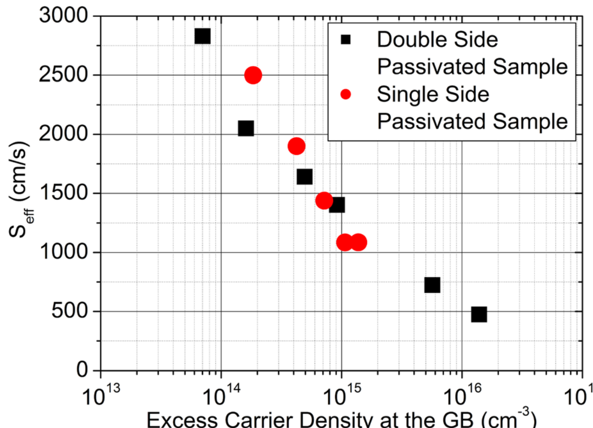

FIG. 8. Injection dependent S_{eff} of GB3, as highlighted in Fig. 6, extracted from a single-side passivated sample and a double-side passivated sister wafer.

excess carrier density and can influence the apparent injection dependence of the extracted S_{eff} values. Moreover, in our model, we assume a constant S_{eff} value for the entire GB. This might not be strictly true for GBs in single-side passivated samples, as the carrier profiles are highly non-uniform depth-wise and the S_{eff} of some GBs can be strongly injection dependent, as shown above. The extracted S_{GB} hence only represents an average surface recombination velocity of a GB over a range of injection levels. Furthermore, due to the infinite surface recombination at the rear surfaces, higher injection densities are difficult to achieve in a single-side passivated wafer even with a high intensity illumination source. This limits the studies of GB behaviour to low or moderate injection levels.

C. Sensitivity studies

In order to determine the limitations of our proposed method for quantifying the recombination strength of a GB, the sensitivity of the PL profile for both double-side and single-side passivated samples is evaluated. In the simulation, we assume that the double-side and the single-side passivated samples have a thickness of $150\,\mu$m and $300\,\mu$m, respectively, similar to the thickness of the mc-Si wafers used in this work after chemical polishing. Both samples are illuminated with the same incident photon flux, $2.7 \times 10^{18}\,\text{cm}^{-2}\text{s}^{-1}$, at 808 nm. Note that even with the same incident photon flux, the injection levels in both samples are different. Firstly, the sensitivity of the PL profile on S_{GB} is investigated, as shown in Fig. 9. The intra-grain bulk lifetimes for both samples are assumed to be injection independent in this simulation and are set to be $300\,\mu$s. For the double-side passivated sample, the PL profile is sensitive to variation in S_{GB} when $S_{GB} \ll 1000\,\text{cm/s}$ and only varies slightly once S_{GB} exceeds $2000\,\text{cm/s}$. This is due to the fact that the recombination rate in the latter case is limited by the transport of carriers to the GB rather than its intrinsic recombination properties. On the other hand, the PL profile in the single-side passivated sample does not saturate when S_{GB} increases, as shown in Fig. 9(b), implying that single-side passivated samples are more suitable to study strongly recombination active GBs.

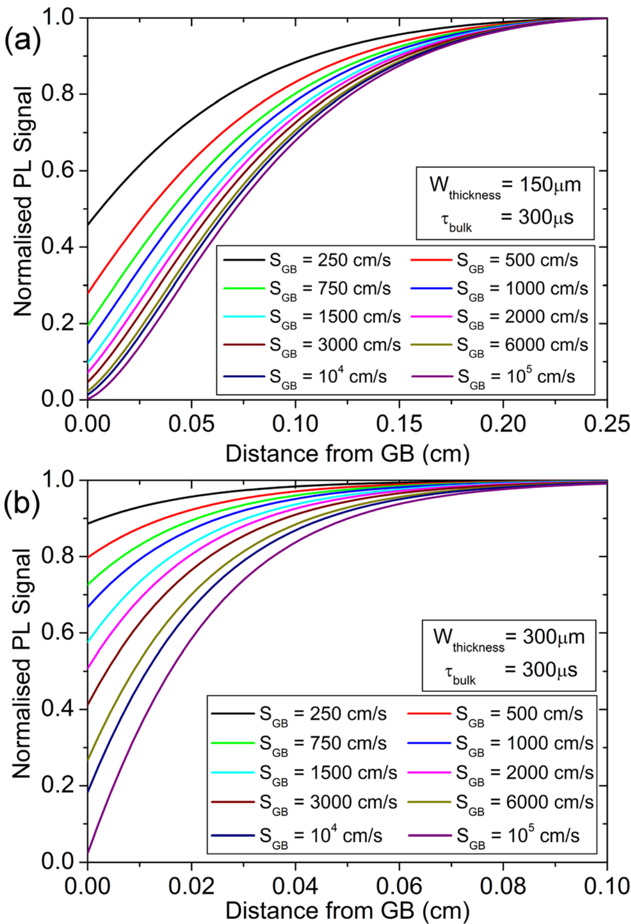

FIG. 9. Sensitivity of PL profile on S_{GB} for a (a) double-side passivated wafer (b) single-side passivated wafer. Only one side of the PL profile is shown as the PL profile is symmetrical. The bulk lifetimes of the neighbouring grains are assumed to be injection independent and are set to be $300\,\mu$s.

Secondly, the sensitivity of the PL profile on the intra-grain bulk lifetime is evaluated. In this simulation, we fix the lifetime on one of the neighbouring grains for reference and then observe the variation of the PL profile while changing the lifetime of the other grain to a certain percentage of the reference grain. Our result, as shown in Fig. 10, shows that the PL profile on a double-side passivated sample is very sensitive to the intra-grain lifetime. A 10% difference in the intra-grain lifetime can significantly change the shape of the PL profile. This suggests that uncertainty in the measured intra-grain lifetime can result in a relatively large uncertainty in the fitting. In contrast, the PL profile on the single-side passivated sample is less dependent on the bulk lifetime. As a result, the fitting will have a higher tolerance for uncertainty in the measured bulk lifetime.

V. CONCLUSION

We present a direct fitting approach based on the steady state photoluminescence (PL) imaging technique and 2D modelling of the PL intensity profile across a GB, to determine the effective surface recombination velocity (S_{eff}) of GBs in multicrystalline silicon wafers. The method is demonstrated on double-side passivated wafers and single-side passivated wafers. The former allows evaluating S_{eff} of GBs

[This article is copyrighted as indicated in the article. Reuse of AIP content is subject to the terms at: http://scitation.aip.org/termsconditions. Downloaded to] IP: 130.56.107.192 On: Thu, 29 Jan 2015 19:35:37

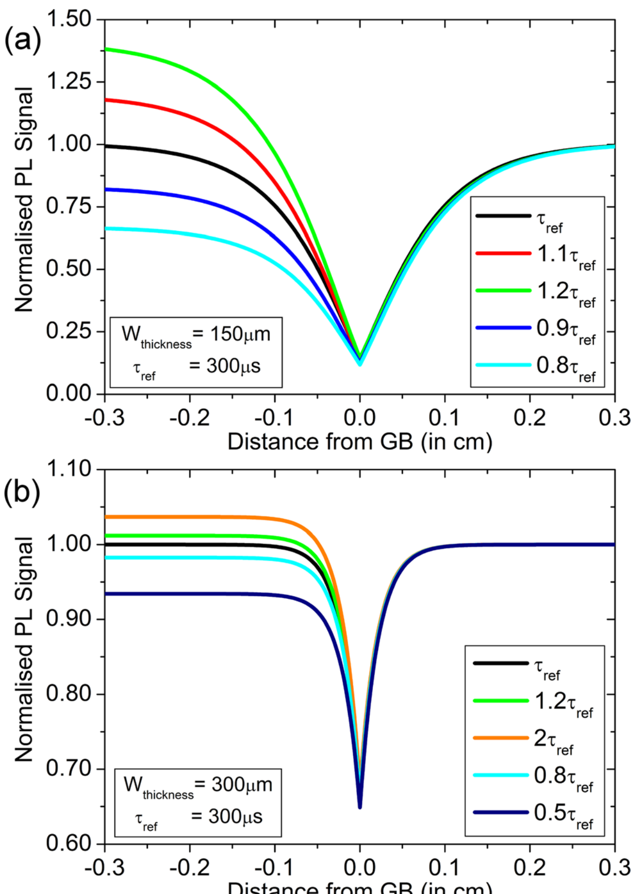

FIG. 10. Sensitivity of PL profile on intra-grain bulk lifetime for a (a) double-side passivated wafer (b) single-side passivated wafer. S_{eff} of the GB is set to be 1000 cm/s. The bulk lifetimes of the reference grains are set to be 300 μs.

as a function of injection level but is limited to less recombination active GBs located between large grains. The latter allows more GBs or even some dislocations to be studied, but only allows extraction of S_{eff} values of GBs at low or moderate injection levels. It also requires a double-side passivated sister sample for extracting the bulk lifetime information in the two neighbouring grains, as required for the analysis. The methods are likely to be particularly useful for quantitatively studying the responses of GBs and dislocation networks to different cell processing steps, such as phosphorus gettering and hydrogenation.

ACKNOWLEDGMENTS

H. C. Sio acknowledges scholarship support from BT Imaging and the Australian Renewable Energy Agency (ARENA). This work has been supported by the Australian Research Council (ARC). The authors also acknowledge the inspiration from simulation program QsCell[25] by Professor A. Cuevas in the modelling of carrier diffusion and photoluminescence.

APPENDIX: MODELLING DESCRIPTION

The semiconductor is divided into multiple nodes in both x and y directions, as shown in Fig. 1(b), for finite element analysis. A summary of the equations used in the modelling is given below.

1. Bulk equations

In 2D and under steady state conditions $(dn_{x,y}/dt = 0)$, the continuity equation can be written as:

$$\frac{dn_{x,y}}{dt} = D_{eff}(n_{x,y}) \times \nabla^2 n_{x,y} + G_{x,y} - \frac{n_{x,y} - n_0}{\tau_{x,y}(n_{x,y})} = 0, \quad \text{(A1)}$$

where x, y denotes the position of the node, $n_{x,y}$ is the excess carrier concentration, $G_{x,y}$ is the local excess carrier generation rate per unit volume, $\tau_{x,y}$ is the local bulk lifetime, n_0 is thermal equilibrium electron concentration, and D_{eff} is the effective carrier diffusivity.[25] $(n_{x,y} - n_0)/\tau_{x,y}(n_{x,y})$ represents the bulk recombination rate. $D_{eff}(n_{x,y}) \times \nabla^2 n_{x,y}$ represents the rate of change of electron current flowing into the node. The electron current, in general, consists of a diffusion term and a drift term, both can be lumped together with the use of D_{eff}.[25] Here, we assume that any space charge regions near the GBs[26] are small in extent in comparison to the minority carrier diffusion lengths, allowing us to avoid modelling the impact of the space charge regions near GBs. In this work, we adapt the carrier mobility model from Klaassen[27,28] to calculate the effective carrier diffusivity, according to:

$$D_{eff} = \frac{(n+p)D_n D_p}{nD_n + pD_p}, \quad \text{(A2)}$$

where D_n and D_p are the diffusion coefficients for electrons and holes.

2. Boundary conditions

Surface recombination acts as another recombination source in the nodes located at the surfaces or at the GB. The continuity equation is modified accordingly to represent those nodes. For a node located at the front surface, Eq. (A1) is modified as,

$$\frac{dn_{x,y}}{dt} = D_{eff}(n_{x,y}) \times \nabla^2 n_{x,y} + G_{x,y} - \frac{n_{x,y} - n_0}{\tau_{x,y}(n_{x,y})} - \frac{S_{front}(n_{x,y} - n_0)}{\Delta y/2} = 0, \quad \text{(A3)}$$

where S_{front} is the effective surface recombination velocity of the front surface. $S_{front}(n_{x,y} - n_0)/\Delta y/2$ represents the recombination rate per unit volume of the node induced by surface recombination at the front surface. Equivalently, the boundary condition for a node located at the GB can be express as,

$$\frac{dn_{x,y}}{dt} = D_{eff}(n_{x,y}) \times \nabla^2 n_{x,y} + G_{x,y} - \frac{n_{x,y} - n_0}{\tau_{x,y}(n_{x,y})} - \frac{S_{GB}(n_{x,y} - n_0)}{\Delta x} = 0, \quad \text{(A4)}$$

where S_{GB} is the effective surface recombination velocity of the GB. $S_{GB}(n_{x,y} - n_0)/\Delta x$ represents the recombination rate per unit volume of the node induced by recombination at the GB. The difference between the volume of the nodes at the front surface and at the GB leads to the factor of 2 difference in the surface recombination terms in Eqs. (A3) and (A4).

[This article is copyrighted as indicated in the article. Reuse of AIP content is subject to the terms at: http://scitation.aip.org/termsconditions. Downloaded to] IP: 130.56.107.192 On: Thu, 29 Jan 2015 19:35:37

3. Implementation

The carrier concentration of each individual node is correlated to the carrier concentration of its adjacent nodes through the $\nabla^2 n_{x,y}$ term in Eqs. (A1), (A3), and (A4) and the boundary conditions $(S_{front}, S_{rear}, S_{GB})$, thus forming a system of equations. The carrier concentration in each node can be determined by solving this system of equations if each local D_{eff}, $\tau_{x,y}$, and $G_{x,y}$ are all known. The local generation rate is calculated based on the incident photon flux, the reflectivity at the front surface and the absorption coefficient of silicon, or otherwise can be obtained from other modelling tools such as OPAL.[29] The effective carrier diffusivity in each element is calculated through Eq. (A2). Note that the effective carrier diffusivity and the bulk lifetime are both injection dependent. This requires an initial guess of the carrier concentration and solving the system of equations through iteration until each local carrier concentration converges. The model is implemented in Matlab. The average computation time is on the order of seconds, depending on the grid size. Of course, it is also possible to use other 2D/3D simulation packages such as Sentaurus[30] to simulate the cases described in this work.

4. Modelling and fitting of the PL signal

The detected PL signal can be modelled based on the local carrier concentration within a semiconductor. The rate of spontaneous emission of electrons and holes via band-band transitions can be expressed by,[31,32]

$$r_{sp}(x,y,\hbar\omega) = \alpha(\hbar\omega) \times \frac{{n_{Si}}^2 \times (\hbar\omega)^2}{\pi^2 \hbar^3 c^2} \times \exp\left(\frac{-\hbar\omega}{kT}\right) \times \frac{1}{{n_i}^2} \times (p_{x,y} n_{x,y}), \quad \text{(A5)}$$

where α is the absorption coefficient for band to band transitions,[33] n_{Si}, $\hbar\omega$, $\hbar$, c denote the refractive index, photon energy, reduced Planck's constant and velocity of light in vacuum, respectively. Accounting for reabsorption and multiple reflections on both surfaces and assuming planar surfaces, the photon flux per energy interval emitted by each individual node into a solid angle of detection Ω is described as,[34]

$$\frac{dj_{\gamma,em}}{d(\hbar\omega)}(x,y,\hbar\omega) = \frac{\Omega}{4\pi} \frac{1 - R_f(\hbar\omega)}{1 - R_f(\hbar\omega) R_b(\hbar\omega) \exp[-2\alpha(\hbar\omega)W]} r_{sp}(x,y,\hbar\omega) \times \{\exp[-\alpha(\hbar\omega)y] + R_b(\hbar\omega) \times \exp[-\alpha(\hbar\omega)(2W - y)]\} \Delta x \Delta y \Delta z, \quad \text{(A6)}$$

with $R_f(\hbar\omega)$ and $R_b(\hbar\omega)$ being the spectral reflectivity of the front and of the rear surface, W being the thickness of the wafer, and $\Delta x \Delta y \Delta z$ represents the volume of the node. The influence of free carrier absorption[35,36] is neglected in Eq. (A6) due to its minor impact and weak wavelength dependence in the inspected wavelength range, coupled with the fact that we use relative PL data. Here, we assume only the photon flux emitted vertically from each node can reach the detector due to the narrow escape cone at the silicon-air interface and the large object distance from the imaging lens which limits the solid angle of detection to within the column dimensions.[37] This assumption can only hold for samples with planar surfaces.[38] The solid angle of detection is assumed to be constant across the sample surface, thus does not impact the relative PL signal. Based on the assumptions above, the PL signal at each pixel in a PL image is modelled by integrating the photon flux emitted vertically from nodes in the same column. The measured relative PL intensity at a given coordinate x can be expressed as:

$$I(x)_{PL,\ measured} = K \times I(x)_{PL,simulated}, \quad \text{(A7)}$$

where

$$I(x)_{PL,simulated} = \int_{hw_1}^{hw_2} \left(Q_{detector}(\hbar\omega) T_{filter}(\hbar\omega) \times \sum_{y=0}^{y=W} \frac{dj_{\gamma,em}}{d(\hbar\omega)}(x,y,\hbar\omega) \right) d(\hbar\omega), \quad \text{(A8)}$$

with $Q_{detector}$ being the quantum efficiency of the silicon detector, T_{filter} being the transmittance of the filters placed in front of the detector and K being a scaling factor. The scaling factor K can be determined by comparing the measured PL signal of a spatially uniform region with the simulated PL signal, calculated according to Eq. (A8). This scaling factor, in principle, is a constant and is homogeneous among different samples. However, due to the fact that the scaling factor is calculated based on various experimental determined parameters such as the reflectivity and the bulk lifetimes which are subject to a certain level of uncertainty, we applied an individual value of K for each sample determined by choosing a spatially uniform region in that particular sample for improving the accuracy of the modelling of the detected PL signal. The average value of the scaling factor K extracted from both single-side and double-side passivated samples presented in this work is 2.8×10^{-7}, with a relative standard deviation of 7%.

Based on Eq. (A7), the detected PL signal at each position x can be calculated if the carrier density inside the semiconductor is known, thus allowing modelling of the PL profile across a GB. A list of parameters required for the fitting is outlined in Table I.

TABLE I. A list of parameters required for the fitting.

Sample parameter	
Spectral reflectivity of the front and rear surfaces	$R_f(\hbar\omega), R_b(\hbar\omega)$
Thickness	W
Doping	N_A
Lifetimes of the neighbouring grains	$\tau_1(\Delta n),\ \tau_2(\Delta n)$
Measurement dependent parameter	
Incident photon flux	ϕ
Transmission of the optical filter	$T_{filter}(\hbar\omega)$
Quantum efficiency of the detector	$Q_{detector}(\hbar\omega)$

[This article is copyrighted as indicated in the article. Reuse of AIP content is subject to the terms at: http://scitation.aip.org/termsconditions. Downloaded to] IP: 130.56.107.192 On: Thu, 29 Jan 2015 19:35:37

[1]P. Karzel, M. Ackermann, L. Gröner, C. Reimann, M. Zschorsch, S. Meyer, F. Kiessling, S. Riepe, and G. Hahn, J. Appl. Phys. **114**, 244902 (2013).
[2]J. Chen, T. Sekiguchi, D. Yang, F. Yin, K. Kido, and S. Tsurekawa, J. Appl. Phys. **96**, 5490–5495 (2004).
[3]H. C. Sio, T. Trupke, S. P. Phang, and D. Macdonald, "Electrical properties of different types of grain boundaries in multicrystalline silicon by photoluminescence imaging," in *Proceedings of the 27th European Photovoltaic Solar Energy Conference, Frankfurt* (2012), pp. 714–718.
[4]T. Buonassisi, A. A. Istratov, M. D. Pickett, M. A. Marcus, T. F. Ciszek, and E. R. Weber, Appl. Phys. Lett. **89**, 042102 (2006).
[5]I. Takahashi, N. Usami, H. Mizuseki, Y. Kawazoe, G. Stokkan, and K. Nakajima, J. Appl. Phys. **109**, 033504 (2011).
[6]S. Joonwichien, S. Matsushima, and N. Usami, J. Appl. Phys. **113**, 133503 (2013).
[7]M. I. Bertoni, S. Hudelson, B. K. Newman, D. P. Fenning, H. F. W. Dekkers, E. Cornagliotti, A. Zuschlag, G. Micard, G. Hahn, G. Coletti, B. Lai, and T. Buonassisi, Prog. Photovolt.: Res. Appl. **19**, 187–191 (2011).
[8]J. Chen, D. Yang, Z. Xi, and T. Sekiguchi, Physica B: Condens. Matter **364**, 162–169 (2005).
[9]Y. Augarten, T. Trupke, M. Lenio, J. Bauer, J. W. Weber, M. Juhl, M. Kasemann, and O. Breitenstein, Prog. Photovolt.: Res. Appl. **21**, 933–941 (2013).
[10]C. Donolato, J. Appl. Phys. **84**, 2656–2664 (1998).
[11]C. Donolato, J. Appl. Phys. **54**, 1314–1322 (1983).
[12]S. Riepe, G. Stokkan, T. Kieliba, and W. Warta, Solid State Phenom. **95–96**, 229–234 (2003).
[13]G. Stokkan, S. Riepe, O. Lohne, and W. Warta, J. Appl. Phys. **101**, 053515 (2007).
[14]R. Corkish, T. Puzzer, A. B. Sproul, and K. L. Luke, J. Appl. Phys. **84**, 5473–5481 (1998).
[15]G. Micard, G. Hahn, A. Zuschlag, S. Seren, and B. Terheiden, J. Appl. Phys. **108**, 034516 (2010).
[16]T. Trupke, R. A. Bardos, M. C. Schubert, and W. Warta, Appl. Phys. Lett. **89**, 044107 (2006).
[17]D. G. Luenberger and Y. Ye, *Linear and Nonlinear Programming*, 3rd ed. (Springer, 2008), Vol. 116.
[18]M. J. Kerr, J. Schmidt, A. Cuevas, and J. H. Bultman, J. Appl. Phys. **89**, 3821–3826 (2001).
[19]A. Cuevas, P. A. Basore, G. Giroult-Matlakowski, and C. Dubois, J. Appl. Phys. **80**, 3370–3375 (1996).
[20]D. Walter, A. Fell, E. Franklin, D. Macdonald, B. Mitchell, and T. Trupke, IEEE J. Photovolt. **4**, 368–373 (2014).
[21]H. C. Sio, S. P. Phang, T. Trupke, and D. Macdonald, Solar Energy Mater. Solar Cells **131**, 77–84 (2014).
[22]S. P. Phang, H. C. Sio, and D. Macdonald, Appl. Phys. Lett. **103**, 192112 (2013).
[23]M. Seibt, R. Khalil, V. Kveder, and W. Schröter, Appl. Phys. A **96**, 235–253 (2009).
[24]S. Bowden and R. A. Sinton, J. Appl. Phys. **102**, 124501 (2007).
[25]A. Cuevas, Energy Procedia **8**, 94–99 (2011).
[26]C. H. Seager, J. Appl. Phys. **52**, 3960–3968 (1981).
[27]D. B. M. Klaassen, Solid–State Electron. **35**, 953–959 (1992).
[28]D. B. M. Klaassen, Solid-State Electron. **35**, 961–967 (1992).
[29]S. C. Baker-Finch and K. R. McIntosh, "A freeware program for precise optical analysis of the front surface of a solar cell," in *35th IEEE Photovoltaic Specialists Conference (PVSC), Honolulu, HI, 20–25 June 2010* (2010), p. 002184–002187.
[30]Synopsys, Sentaurus Device User Guide, Version 2013.03 (2013).
[31]P. Würfel, J. Phys. C: Solid State Phys. **15**, 3967 (1982).
[32]P. Würfel, S. Finkbeiner, and E. Daub, Appl. Phys. A **60**, 67–70 (1995).
[33]M. A. Green, Solar Energy Mater. Solar Cells **92**, 1305–1310 (2008).
[34]K. Schick, E. Daub, S. Finkbeiner, and P. Würfel, Appl. Phys. A **54**, 109–114 (1992).
[35]B. Mitchell, J. Greulich, and T. Trupke, Solar Energy Mater. Solar Cells **107**, 75–80 (2012).
[36]D. K. Schroder, R. N. Thomas, and J. C. Swartz, IEEE J. Solid-State Circuits **13**, 180–187 (1978).
[37]A. Fell, D. Walter, S. Kluska, E. Franklin, and K. Weber, Energy Procedia **38**, 22–31 (2013).
[38]M. C. Schubert, S. Pingel, M. The, and W. Warta, J. Appl. Phys. **101**, 124907 (2007).

[This article is copyrighted as indicated in the article. Reuse of AIP content is subject to the terms at: http://scitation.aip.org/termsconditions. Downloaded to] IP: 130.56.107.192 On: Thu, 29 Jan 2015 19:35:37